The International Journal of Advanced Manufacturing Technology (2023) 129:2921–2931
https://doi.org/10.1007/s00170-023-12505-8

ORIGINAL ARTICLE

Microstructural evolution and mechanical properties of rapidly solidified thin-strip continuous cast AA5182 Al-Mg alloy under varying heat inputs in friction stir welding

Hesam Pouraliakbar[1] · Hamed Jamshidi Aval[2] · Andrew Howells[3] · Mark Gallerneault[4] · Vahid Fallah[1]

Received: 13 July 2023 / Accepted: 9 October 2023 / Published online: 19 October 2023

Abstract
Rapidly solidified thin-strip (TS) continuous cast AA5182 Al-Mg alloy was welded for the first time by the friction stir welding (FSW) technique. The response of solute supersaturation that formed during TS casting to thermomechanical processing during FSW was investigated. The analysis demonstrated that the re-precipitation of the intergranular β-Al_3Mg_2 was strongly affected by weld heat input. Similarly, the microstructural evolution associated with FSW significantly impacted mechanical behavior. It was observed that heat generation results in the formation of a high volume of β-Al_3Mg_2 intermetallic particles and tunneling defects at the advancing side of the stir zones, as well as grain coarsening. Mitigation of solute supersaturation in the stir zone, linked to excess β-phase evolution and consequently solute depletion in the aluminum matrix, was manifested as the simultaneous work-hardening and ductility decline as well as in the stress drop of inhomogeneous plastic flow observed in the tensile specimens.

Keywords Thin-strip cast · Rapid solidification · AA5182 Al-Mg alloy · Solute supersaturation · Friction stir welding (FSW) · Heat input · Mechanical properties

1 Introduction

Recently, Hazelett-CASTechnology™ has introduced a new method of fabricating aluminum sheets in the thickness range of 2–5 mm via thin-strip (TS) casting. By casting with a thin cross-section, the TS process route eliminates the need for intermediate processing steps including "scalping," "homogenization," and "hot-rolling," as well as any major "cold-rolling" step which are necessary for the conventional production route, e.g., those utilizing the Direct Chill (DC) casting technique [1, 2]. In this energy-saving and cost-effective strategy, molten metal continuously passes through cooling belts and solidifies uniformly at a high rate [3]. Higher quenching rates due to the reduced melt thickness generally lead to a finer microstructure, less solute microsegregation, and ultimately a higher solute supersaturation in the matrix [4–6].

Al-Mg-based alloys (AA5xxx) are commonly used for many structural applications due to a desirable combination of formability, weldability, corrosion resistance, and medium strength [7–10]. Mg, as inferred by the binary Al-Mg phase diagram [11], has a solid solubility limit of ~17 wt% (at 450 °C) dropping to just below 2 wt% at room temperature, i.e., the aluminum lattice has to re-distribute Mg atoms upon cooling from the melting point to its ultimate freezing point. Al-Mg alloys with Mg > 5.5 wt% can present processing challenges due to the formation of a considerable amount of non-equilibrium β-Al_3Mg_2 eutectic phase rendering the material susceptible to ingot cracking, challenges during homogenization, dissolution of the β-phase, and post-processing issues such as intergranular cracking (IGC) and stress corrosion cracking (SCC) [12–14]. Because of the higher solidification rate in TS strips which was reported

✉ Hesam Pouraliakbar
h.pouraliakbar@queensu.ca

1 Azar Advanced Manufacturing Laboratory (AAML), Department of Mechanical and Materials Engineering, Queen's University, Kingston, ON K7L 3N6, Canada

2 Department of Materials Engineering, Babol Noshirvani University of Technology, Shariati Avenue, Babol 47148-71167, Iran

3 Hazelett-CASTechnology, 800 Innovation Dr., Kingston, ON K7K 7E7, Canada

4 Department of Mechanical and Materials Engineering, Queen's University, Kingston, ON K7L 3N6, Canada

to be ~100 times greater than that for DC casting [3], the formation of the intergranular β-phase is likely to be different from conventionally produced material. For example, a higher level of solid solution Mg might be expected in TS samples which is beneficial from the uniformity of the primary phase and work-hardening perspective.

While there has been extensive research on the evolution of intermetallics in Al-Mg alloys using various processing methods, there is limited discussion specifically focused on the microstructure evolution in AA5182 alloy [8]. Moreover, when considering friction stir welding (FSW), a reliable alternative in solid-state joining and thermomechanical processing, as the processing method for AA5182 alloy, the number of studies in this area is even more limited. Most literature related to FSW predominantly explores topics such as grain size evolution in the stir zone or heat-affected zone (HAZ) and their impact on mechanical properties, residual stresses, and, to some extent, the corrosion behavior of welded joints [15–21]. However, there is a scarcity of literature that pays direct attention to the evolution of intermetallics, especially β-phase, in AA5182 alloy within FSW. Nonetheless, major aspects of mechanical properties and corrosion resistance in Al-Mg alloys are directly linked to the β-phase [22, 23].

Welding is often an inevitable fabrication step in the transportation industry, and it is imperative that one needs to investigate the effect of its input parameters on newly developed alloys [24–26]. In the context of AA5xxx alloys, a significant portion of the published work focuses on dissimilar welding of these alloys with other aluminum alloy series (AA1xxx, AA2xxx, and AA6xxx) or other alloying systems in which the formation of defects and mechanical properties takes precedence [17–19]. Most prior research and literature on FSW have concentrated on wrought Al-Mg alloys. Traditional casting techniques produce ingots that require intermediate processing steps (e.g., hot-rolling and cold-rolling) to produce sheets suitable for welding. However, this study introduces the novel approach of TS casting, which directly produces strips that can be utilized for welding without any preceding processing steps.

Another distinctive aspect of the current study is that the alloy used (i.e., TS AA5182) is welded in its as-cast condition without prior treatment or homogenization. As indicated earlier, the new caster enables rapid solidification cooling rates which is a significant improvement compared to conventional casting methods. The TS casting as a rapid continuous casting process effectively retains solute atoms, particularly magnesium (Mg) atoms in AA5182 alloy, within the aluminum matrix. This retention leads to a state of supersaturation and suppresses the formation of eutectic phases (e.g., β-phase) and intermetallic compounds (e.g., Al-Mn-Fe). Preserved level of solutes within aluminum suggests the possibility of achieving heat-treatable properties in TS alloy. Consequently, the application of FSW has the potential to trigger unique transformations in this material that have not been previously identified or documented. Here, the feasibility of FSW was studied, and the response of solute supersaturation in as-cast TS AA5182 strip to the weld heat input was explored for the first time to pave the way for future studies.

2 Experimental

The TS AA5182 strip was cast at 3 mm thickness and 350 mm width using a CASTechnology-Hazellett™ strip caster under a numerically estimated solidification cooling rate of ~10^3 K/s [3]. Strip samples of 100 × 150 × 3 mm^3 dimension with a bulk chemical composition given in Table 1 were employed for butt joining. The chemical composition was acquired from various depths within the strip through the application of the spark optical emission spectroscopy (Spark-OES) technique (Spectro Analytical Instruments, SPECTROMAXx LMX09). The data presented in Table 1 represents an average compilation of the results obtained from this analysis. FSW was conducted using a custom-built machine featuring a 30 kW primary motor with the capacity to provide torque of up to 150 N.m. The machine, which is outfitted with a control system, permits the adjustment of the spindle rotational speed, the workpiece traverse speed (i.e., linear welding speed), and the recording of spindle torque through the utilization of the motor's electrical signals. Consequently, all essential parameters for calculating heat input are collected through the control system. A conical H13 tool with a square frustum probe has a shoulder diameter of 18 mm and a pin length of 2.8 mm. A schematic representation of the designed pin, including its specific measurements, is given in Fig. 1. To control the temperature and heat input during welding, a K-type thermocouple was inserted in the weld line. FSW was carried out using rotational speeds of 400, 800, and 1200 rpm and a traverse of 40 mm/min. The applied axial pressure as well as plunge depth (0.2 mm) were constant in all trials. The samples were cut perpendicular to the joint line, and the cross-sections were studied by optical microscopy (OM) and scanning electron microscopy (SEM, FEI NanoSEM

Table 1 Examined chemical composition for TS AA5182 alloy

Chemical composition (wt%)						
Al	Mg	Mn	Fe	Si	Zn	Cu
Bal.	4.41 ± 0.13	0.24 ± 0.003	0.12 ± 0.005	0.05 ± 0.002	0.03 ± 0.003	0.01 ± 0.002

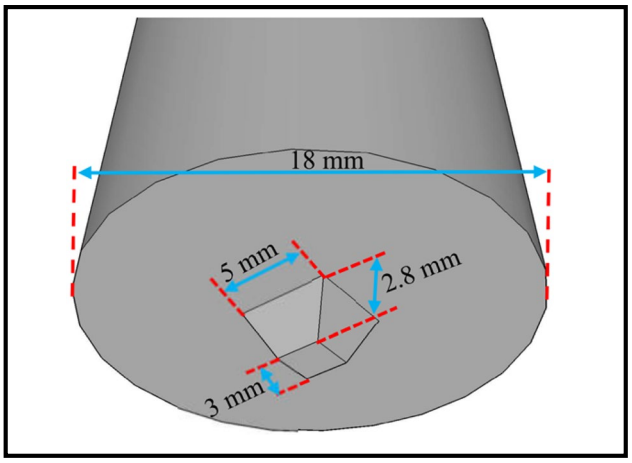

Fig. 1 The schematic representation of the applied tool for FSW of TS AA5182 samples

450) techniques. A modified Poulton's solution was used to reveal the microstructure. The mechanical properties of the joints were examined by ASTM-E8 standard tensile test coupons machined from stir zones parallel to the welding lines at an initial straining speed of 1 mm/min.

3 Results and discussion

Figure 2 illustrates the optical micrographs (OM) obtained from a cross-section of the FSWed specimens perpendicular to the weld line, and the numbered images correspond to the identified regions in the figure. Figure 2(a-c) exhibits that increasing the pin rotation speed, and thus the corresponding excess heat generation, expands the stir zone in which dynamically recrystallized (DRX) grains emerge within the thermomechanically processed region under severe plastic deformation (see the refined grain structures vs. the original microstructure shown for locations 1–3 vs. 4, respectively). Several studies have emphasized the impact of stir zone grain size on the weld metal mechanical properties and the role of the heat input as its main determinative [24, 27, 28]. Figure 3 shows the variation of average grain size, peak temperature, and area in stir zones by heat input calculated from the following equation [29]:

$$\text{Heat input}\left(\frac{j}{\text{mm}}\right)=\eta\left(\frac{\omega.T}{v}\right) \quad (1)$$

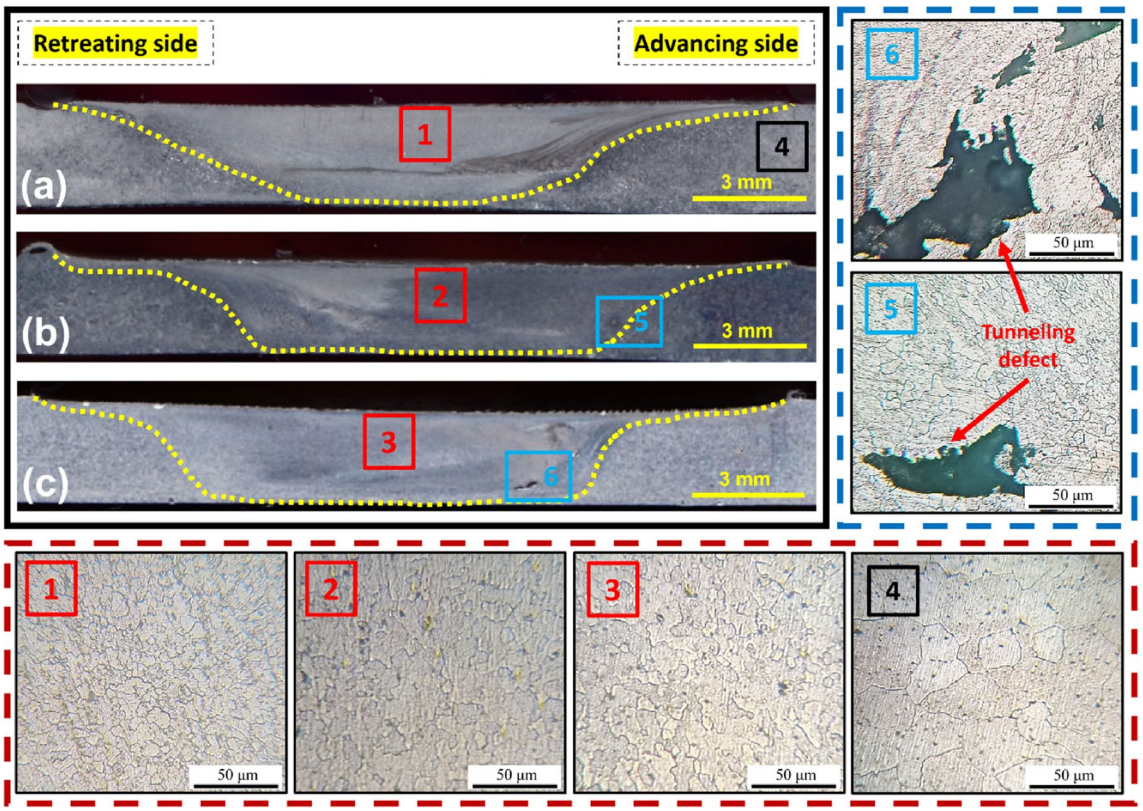

Fig. 2 Examined stereo-OMs from cross-sections of (**a**) 400rpm–40mm/min, (**b**) 800rpm–40mm/min, and (**c**) 1200rpm–40mm/min FSWed samples. Numbered OM images obtained from corresponding locations (**a**–**c**) reveal the microstructure evolution and tunneling defect formation

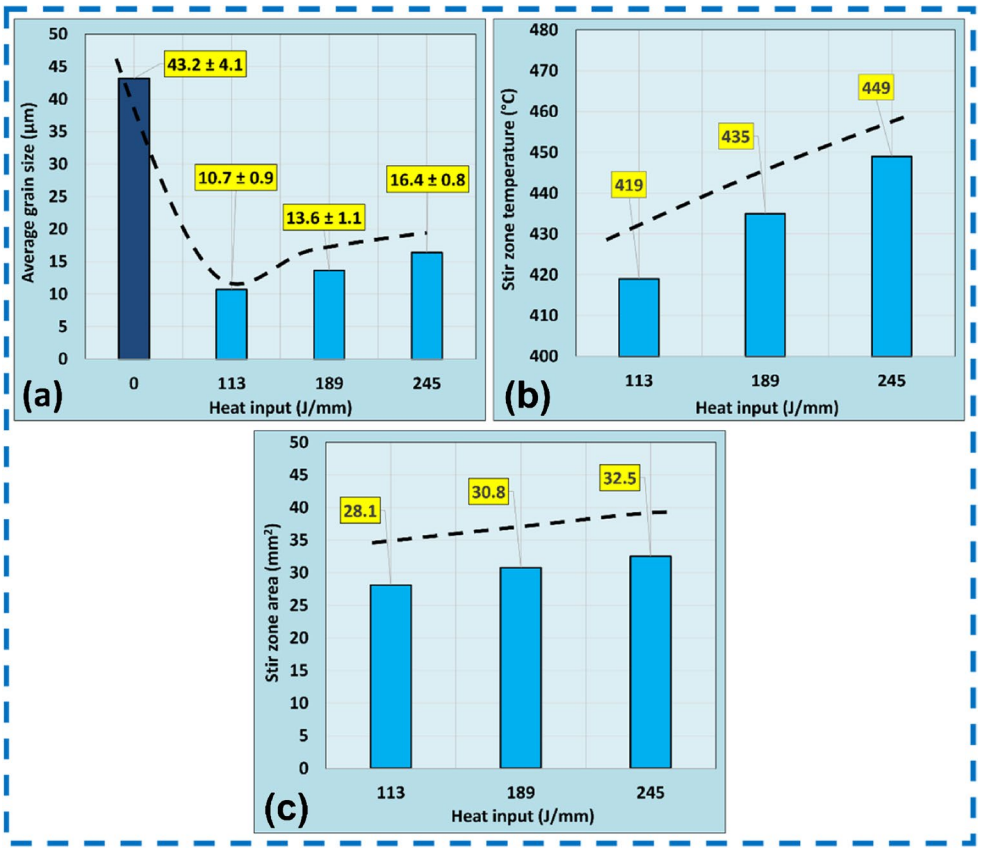

Fig. 3 Variation of **a** average grain size, **b** peak temperature, and **c** area in stir zone by heat input

$$\omega = \left(\frac{2\pi r}{60}\right) \tag{2}$$

where "ω" is the rotational speed (rpm), "η" is the efficiency of heat transfer (~0.9), "ν" is the traverse speed (mm/min), and "T" is the torque (N·m).

Using the control system of the FSW machine, torque values of 12.56, 10.50, and 9.07 N.m were recorded by adjusting the spindle speed to 400, 800, and 1200 rpm, respectively. Employing the provided equations (i.e., Eq. 1 and Eq. 2), the heat input for pin rotations of 400 rpm, 800 rpm, and 1200 rpm were determined as 113, 189, and 245 J/mm, respectively. The excess heat generated by friction caused grain growth and, from OM image analysis, values of 10.7 ± 0.9, 13.6 ± 01.1, and 16.4 ± 0.8 μm were estimated for the mean size of equiaxed DRX grains in the stir zones following the heat input increase. Considering the average grain size of 43.2 ± 4.1 μm in the as-cast alloy, FSW displayed a structural refining potential. Likewise, the stir zone peak temperature and area were affected by the friction heat from the rotating pin and the plastically deformed material. A wider stir region is achieved due to a temperature increase that yields lower flow stress and facile deformation [24, 30]. The generated heat together with the imposed plastic deformation determines the kinetics of DRX and, therefore, controls the microstructure evolution in the stir zone. The combination of grain growth from an increase in heat input and the applied strain by the pin demonstrate the impact of temperature versus deformation. Unlike the peak temperature, the grain growth is not linear with the heat input, particularly from 189 to 245 J/mm (as can be seen in Fig. 3a, b). It is suggested that this is due to the formation of intergranular phases in the stir zone that interfere with the migrating grain boundaries. Stereo-OMs in Fig. 2(b-c) depict the formation of tunneling defects at spots denoting 5 and 6, respectively, at the advancing side of the welds. These defects are caused by the excess heat that induces turbulence in the flow of the severely plasticized metal and, at the same time, prevents the zone behind the tool from getting filled by material. No defects were detected in welds utilizing a 400 rpm rotation (Fig. 2(a)), implying an adequate balance between the applied process parameters. It has been demonstrated that tunneling defects, by further stress concentrations, can exacerbate the mechanical properties of the weld metal subjected to loading [31–33].

Figure 4a–h illustrates the SEM images from the as-cast and weld metals at different magnifications. Figure 4a, b displays the as-cast structure obtained from the mid-thickness region showing coarse aluminum grains and two grain-boundary (intergranular) intermetallics consisting of eutectic β-Al_3Mg_2 (black-phase with blue arrows) and Al_6(Mn,Fe) (white-phase with yellow arrows) phases with

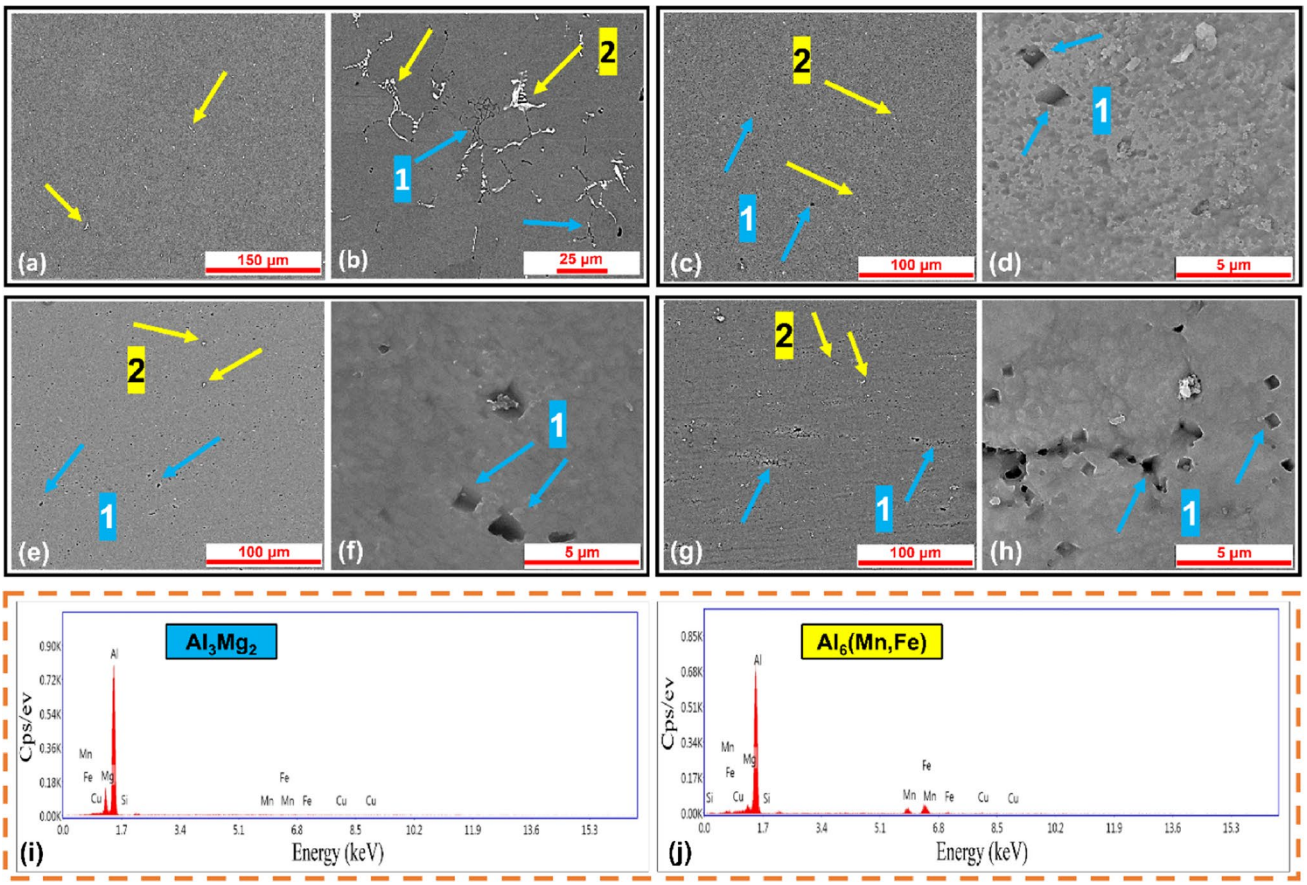

Fig. 4 SEM images obtained from stir zone of **a**, **b** as-cast, **c**, **d** 400 rpm–40mm/min, **e**, **f** 800 rpm–40mm/min, and **g**, **h** 1200 rpm–40 mm/min specimens with different magnifications showing the distribution and morphology of formed intermetallics and **i**, **j** SEM-EDS spectra obtained from β-Al_3Mg_2 (1-blue arrow) and Al_6(Fe,Mn) (2-yellow arrow) particles, respectively, in the as-cast sample

distinct morphologies. Microscopy observations revealed that the size, volume fraction, and morphology of intergranular phases vary through the thickness of the as-cast TS sheet and are affected by the local thermal history (i.e., solidification cooling rate) and microsegregation. For Al-Mg alloys containing Fe, Mn, and Si, the formation of a variety of intergranular phases has been reported in their as-cast and heat-treated states mainly including Al_3(Fe,Mn), Al_6(Mn,Fe), Al_x(Fe,Mn), β-Al_3Mg_2, β-Al_5(Fe,Mn) Si, and α-Al(Fe,Mn) Si intermetallics as well as possibly the Mg_2Si secondary phase [8, 9, 34–36]. It is indicated that in low-Si alloys, the emergence of Si-bearing phases such as Mg_2Si is unlikely, and the Fe/Mn ratio in the alloy would affect the evolution of intermetallics. It is also stated that it would be rather hard to clarify the exact stoichiometry of Al-(Mn,Fe) intermetallics in Mg-containing 5xxx alloys [9, 35, 36]. Furthermore, the occurrence of further transformations during thermomechanical processes may lead to the formation of secondary phases [8, 36]. Microscopy observations from the TS strip revealed that near-surface regions mainly contained fine, needle-like intergranular Al-(Mn,Fe) intermetallics along with sparsely distributed and short β-Al_3Mg_2 eutectic intermetallics. Moving closer to the mid-thickness regions (see Fig. 4b), in addition to centerline solidification shrinkage porosity, the volume fraction of β-Al_3Mg_2 increases considerably, and a coarser evolution of Al_6(Mn,Fe) emerges having a Chinese script appearance. The Mg supersaturation in the Al matrix is therefore likely greater in near-surface areas where there is less time available for diffusion due to a faster solidification and thus the suppression of the eutectic β-Al_3Mg_2 formation kinetics. In contrast, the volume fraction of the eutectic β-Al_3Mg_2 increases towards the mid-thickness which is in line with the solidification cooling rate gradient. Neither Mg_2Si secondary phases nor any of the typical Si-bearing eutectic intermetallics were detected in the as-cast state. In addition to their crystallography, the volume fraction, size, and morphology of the intergranular phases can influence the mechanical properties. Due to higher surface energies, triple junctions are more favored with intermetallics either in the examined cast structure or in the weld samples [37]. Grain boundary wetting phenomena during phase transitions and their impact on the

microstructure evolution and mechanical behavior have been extensively studied in various alloying systems [37, 38].

FSW, by imposing plastic deformation and crushing the grains and intermetallic phases, refines the microstructure. From Fig. 4c–h, severe straining by increasing the pin speed and excess heat generation refined the grain structure and modified the volume fraction and morphology of the intergranular phases. In particular, a high number density of semi-spherical Al_6(Mn,Fe) particles was detected with relatively no total volume change in all welds (i.e., with respect to the as-cast state). This is probably due to the particles not undergoing any dissolution and/or re-precipitation due to their high melting point. For β-Al_3Mg_2, both morphology and volume fractions have altered noticeably. From Fig. 3b, the stir zone peak temperature depending on the pin speed reaches a value of 419–449 °C which (according to the equilibrium Al-Mg phase diagram) exceeds the maximum solid-solubility of Mg in Al for the Al-5%Mg composition. The stir zone temperature is therefore sufficient to cause the dissolution of Mg atoms into the aluminum matrix, followed by a re-precipitation of fine β-Al_3Mg_2 with distinct size and appearance upon cooling. Even for those samples welded at 400 rpm with a corresponding recorded peak temperature of 419 °C, the morphology of the β-Al_3Mg_2 particles detected in the stir zone was polygonal, which is consistent with their tetragonal crystalline structure and incoherent interfaces with the aluminum matrix. These results confirm that the as-cast morphology of β-Al_3Mg_2 has completely disappeared in the weld samples. Re-precipitation of new β-Al_3Mg_2 particles was indeed induced by severe deformation and assisted by rearrangement of dislocations during DRX and the emergence of fine grains inside the stir regions. By increasing the pin speed and heat generation, as evident from Fig. 4d, f, h, the volume fraction of the polygonal β-Al_3Mg_2 was significantly increased with no measurable change in the particle size, i.e., all particles were finer than those in the as-cast sample. Simultaneous dissolution and re-precipitation occurred in response to the applied thermomechanical process and the aluminum matrix diluted by Mg atoms. It appears that the re-precipitated particles have mainly accumulated along the grain boundaries (as evident from Fig. 4h) which weakens the grain boundaries by their incoherent interfaces. It has been shown by Chang et al. [39] that fraction enhancement and accumulation of fine Al-Mg intergranular particles lead to a higher Zener pressure and therefore a decline in the grain growth rate, which is consistent with the observed reduction of growth rate slope in Fig. 3a towards the highest excess heat generation. It is noteworthy to mention that unlike the pattern observed for the intergranular phases in the as-cast microstructure, the distribution of fine particles in the stir zones is found to be uniform throughout the sheet thickness as well as within the width of the weld zone. Figure 4g, h shows the higher density of polygonal particles decorating the aluminum grains boundaries providing a connected network of particles that can assist crack growth, i.e., by providing preferential propagation paths during loading and/or stress crack corrosion. According to the literature, the effect of the particle concentration on the grain boundary can deteriorate the corrosion resistance to a large extent which is referred to as sensitization caused by an intergranular anodic β-Al_3Mg_2 [12, 40]. Several studies correlated the fraction and size of β-Al_3Mg_2 with severe IGC and lower mechanical properties [41–43].

Figure 5a shows the engineering tensile stress-strain curves obtained for the as-cast and FSW specimens, and the numbers in each graph correspond to the examined specimen. The sub-size coupons of the weld samples were cut from the stir zone along the weld line denoting that considering the utilized dimensions, the whole tensile specimens only included the weld metals. Several tensile specimens were examined for each condition to ensure the repeatability of the results, and those presented in Fig. 5 are from a select specimen of each type. From stress-strain curves, heterogeneous/unstable plastic flow (known as the Portevin-Le Chatelier (PLC) effect) was observable for both as-cast and FSW specimens. The PLC effect is extensively studied in Al-Mg alloys, and the effect of Mg solute atoms is well elaborated [44, 45]. Figure 5b shows the collection of the magnified plastic flows during early work-hardening steps including the engineering strain range of $\Delta\varepsilon = 2–6\%$ and stress increment of $\Delta\sigma_{2–6\%} = 50$ MPa. It is trivial that the select $\Delta\varepsilon$ in each sample gives a distinguished magnitude of strength; however, the range of stress variation was kept constant in Fig. 5b for the consistency of the flow stress analysis. Figure 6 displays the fractography micrographs from the fracture surface of tensile samples with different magnifications. From the tensile results (see Fig. 5a), FSW samples with 400 rpm pin speed exhibited the highest yield strength (YS), ultimate tensile strength (UTS), and elongation of 165 MPa, 310 MPa, and 23.01%, respectively. Comparing the corresponding values of 112 MPa, 219 MPa, and 10.22% obtained for the as-cast sample with those for weld samples, the FSW by tuning and refining the microstructure successfully improved both strength and ductility. Due to the associated grain evolution mechanism of DRX in FSW, the dislocation density in the thermomechanical region is likely not high enough to play a role in strengthening; hence, it is believed that Hall-Petch strengthening was the predominant mechanism in the examined strength trend. Increasing the rotation speed decreased the YS and UTS to 145 MPa and 281 MPa for welds by 800 rpm, and 132 MPa and 194 MPa for welds by 1200 rpm rotation, following the grain growth trend obtained for these specimens. No ductility improvement was observed for the samples following the strength

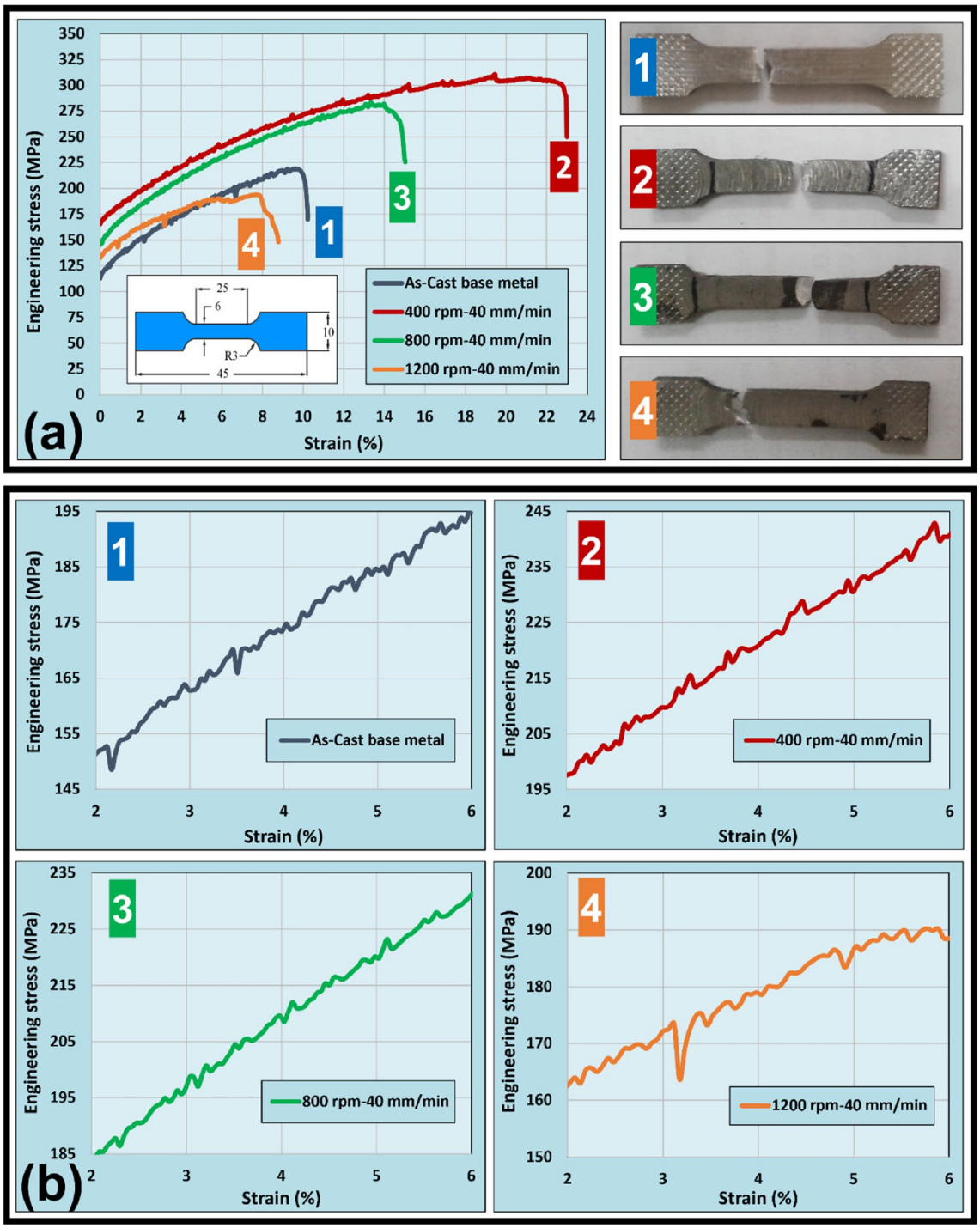

Fig. 5 **a** Engineering stress-strain curves of examined specimens along with the select tensile specimen view showing the fracture location lies within the gauge and **b** magnified representation of inhomogeneous plastic flow (i.e., PLC effect) for the strain range of 2–6% in tensile curves

decrease; this is in contrast to the usual strength-ductility trade-off that takes place in alloys. This is possibly due to the significant effect of the grain boundary weakening by β-Al_3Mg_2 re-precipitation which may have assisted dimples to coalesce and/or crack to propagate under loading (i.e., as evident from the fracture surfaces shown in Fig. 6b–d). Fracture surfaces of weld samples did not exhibit slip, which would have been an indication of ductile fracture, and the dimple formation was believed to be the prevailing fracture mechanism.

From stress-strain curves in Fig. 5a, the difference in elongation-to-failure in the weld samples at 400 rpm and 800

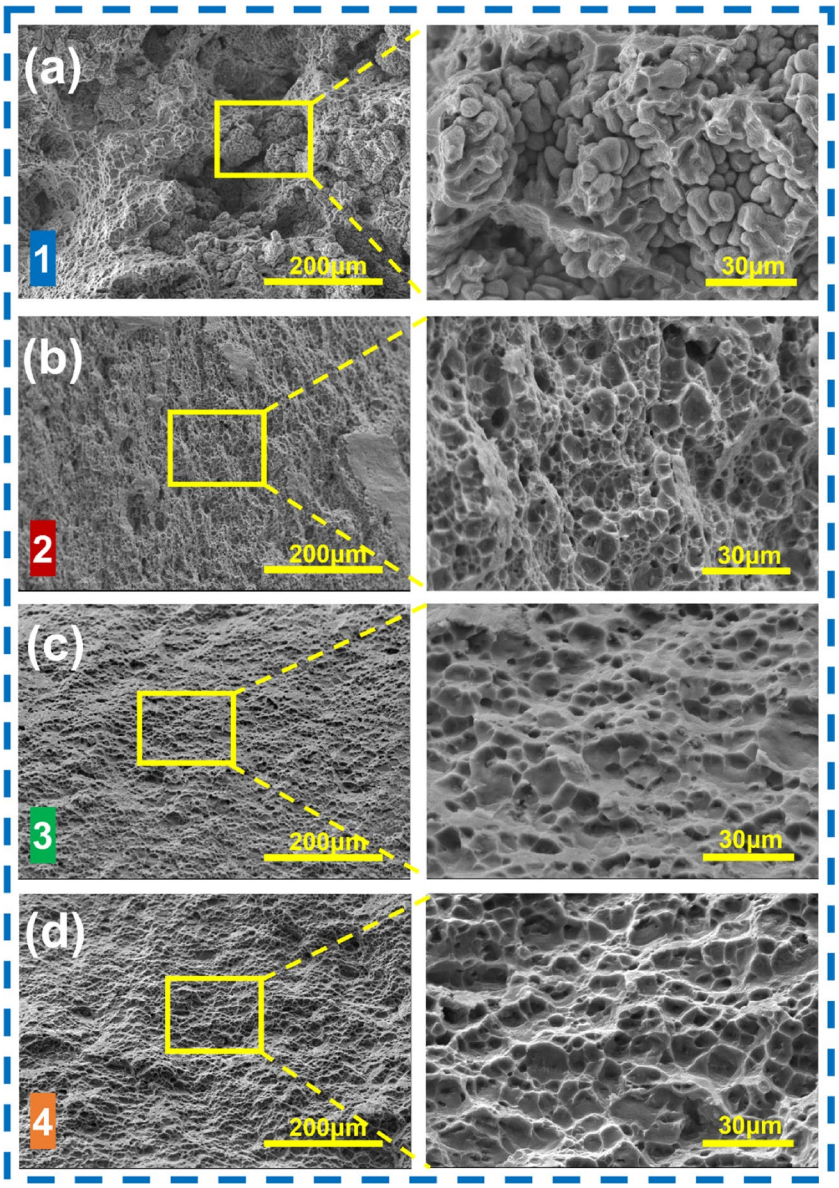

Fig. 6 SEM fractography from fracture surfaces of tensile samples of **a** as-cast TS, **b** 400rpm–40mm/min, **c** 800rpm–40mm/min, and **d** 1200rpm–40mm/min (numbers correspond to the tensile samples in Fig. 5a)

rpm was greater, implying that the early failure was likely caused by fine intergranular particles. This effect is greater for the 1200 rpm sample with a UTS value less than that for the as-cast TS sample. It is believed the minimum UTS and lowest elongation in 1200 rpm specimens are associated with matrix solute depletion and a higher number density/interconnectivity of grain boundary particles. The early tensile failure in the weld samples was in line with fractography surface roughness. From SEM images acquired from fracture surfaces in Fig. 6(b-d), finer dimples and smoother surfaces were formed in the 400 rpm specimen whereas the coarsest dimples and the roughest surfaces were formed in the 1200 rpm specimen. The formation of finer dimples is interdependent with finer grains in the microstructure, and by deferring the crack propagation, higher ductility and toughness are obtained. Fracture surface morphology for the as-cast sample (Fig. 6a) shows interdendritic separation/rupture features in mid-thickness regions as well as dimple structures showing up mostly in the near-surface areas. The interdendritic appearance of the fracture surface is likely related to the presence of centerline shrinkage porosity in the as-cast sample. In contrast, the dimple structure was the only feature observed in the fracture of the weld samples. Considering the employed gauge size of tensile samples, which were smaller than the width of the stir zones, care was taken to ensure that the tunneling defects did not fall within the tensile specimens; hence, the decline in strength and ductility for examined 800 rpm and 1200 rpm samples here is not impacted by the tunneling defects.

Weld samples are also distinct in terms of their work-hardening behavior. As an indicator of work-hardening capacity ($\Delta\sigma_{(UTS\text{-}YS)} = \sigma_{UTS}\text{-}\sigma_{YS}$), $\Delta\sigma_{(UTS\text{-}YS)}$ of about

145 MPa, 136 MPa, 62 MPa, and 105 MPa were obtained for 400 rpm, 800 rpm, 1200 rpm, and as-cast specimens, respectively; the higher the pin speed, the lower the work-hardening capacity in the welds. The lower work-hardening potential could be explained by an early failure associated with an insufficient volume of scattered obstacles (e.g., coarser grain structure in the 1200 rpm sample) to impede the glide of deformation-induced mobile dislocations, thereby allowing for their facile pile-up and thus nucleation of microcracks. This is consistent with a solute-depleted aluminum matrix (due to re-precipitation of a higher amount of intergranular β-Al_3Mg_2 particles) at the higher pin speed samples, which would reduce the dislocation-atom interactions inside the grains. The presence of obstacles in front of the gliding dislocations shortens the free motion distance and affects both the work-hardening potential and the homogeneity of plastic flow. Magnified curves in Fig. 6b illustrate distinct plastic flow patterns for the examined samples, i.e., a less severe serrated flow was observed for weld samples compared to the as-cast sample. This is likely related to the uniformity of the microstructure in the stir zone, grain size, and intergranular phase distribution. Moreover, a more stable flow with attenuated stress drops was observed in the weld samples, especially for 400 rpm and 800 rpm with small repetitive steps of no serration. These no-serration steps are generated by easy dislocation glides with no and/or less strong obstacles in their path due to matrix solute depletion [46, 47]. Sudden stress drops in the 1200 rpm sample are believed to correspond with microcrack formation especially when an accumulation of particles exists at the boundaries (i.e., independently of the dislocation-atom interactions). The most irregular flow was observed in the as-cast TS sample. Furthermore, no yield point extension (YPE) (i.e., Lüdering is known as a type of deformation heterogeneity in alloys) emerged in tensile specimens of weld samples which is prevalent for thermally recrystallized Al-Mg alloys that have undergone severe plastic deformation via cold-/hot-rolling [48]. Given the applied tensile strain rate with uniformly refined grains in the stir zones, it is surmised that the finer grain size combined with the particular dislocation structure formed in the processed zones during DRX affects the dislocation-atom interactions and prevents the emergence of YPE. Hence, the conditions for the formation of deformation bands (Lüders band propagation) were not satisfied in the grains that evolved in weld metals.

The analysis of microstructure evolution along with the examined tensile properties revealed that precautions should be made using FSW of TS AA5182 alloy. That is, consideration of the extent of Mg supersaturated in the aluminum matrix, finer grains, and intergranular phases as compared to their conventional counterparts cast with slower cooling rates. It is believed that the overall lower volume fraction of intergranular β-Al_3Mg_2 eutectic with a finer morphology can be more readily dissolved by the frictional heat during FSW and is subsequently re-precipitated as fine intergranular particles. This is in contrast to alloys containing a larger volume of coarser intergranular β-Al_3Mg_2 eutectic, as their complete dissolution and re-precipitation may not be feasible with the same applied welding variables. Therefore, the detrimental impact of β-Al_3Mg_2 re-precipitation could be a significant issue, which must be addressed by adjusting for the optimum balance in process variables (most notably pin rotation and traverse speed), i.e., to minimize the heat input and to achieve adequate strength-ductility trade-offs in response to further loadings.

4 Conclusions

The effect of heat input during FSW on the microstructure evolution and mechanical properties of the as-cast TS AA5182 Al-Mg strip with solute supersaturation was explored for the first time. The main outputs are summarized as follows:

- Microstructure studies demonstrated that the temperature dominated the plastic deformation influence, leading to the formation of equiaxed DRX grains within the stir zone.
- Increased heat input caused more β-Al_3Mg_2 particles to re-precipitate along grain boundaries. This affected the aluminum matrix enriched with Mg by the thermomechanical process in FSW. The absence of non-polyhedral β-phase in weld metals suggested its complete dissolution due to frictional heat.
- The formation of β-Al_3Mg_2 particles, matrix solute depletion, and grain coarsening due to heat input led to decreased strength and work hardening. Samples processed at 1200 rpm contained a notable amount of β-phase, resulting in reduced ductility and UTS. The decline in mechanical properties was linked to the weakening influence of the β-phase. The welds exhibited greater YS compared to the as-cast sample, suggesting that Hall-Petch strengthening was the sole contributing factor.
- Ascribing the stress drop as being due to unstable plastic flow was consistent with solute dilution and intergranular phase fraction. It is concluded that a minimum heat input should be applied to establish an adequate strength-ductility trade-off. This is consistent with the β-phase re-precipitation in the rapidly solidified TS AA5182 strip compared to conventionally cast counterparts.

Author contribution Hesam Pouraliakbar: formal analysis, data curation, investigation, writing—original draft. Hamed Jamshidi Aval: experimental design, methodology, investigation, writing—review and editing. Andrew Howells: formal analysis, resources, writing—review and editing. Mark Gallerneault: formal analysis, resources, writing—review and editing. Vahid Fallah: conceptualization, methodology, data curation, writing—review and editing, supervision.

Funding and acknowledgment The authors appreciate Hazelett-CASTechnology™ for their financial support and provision of research facilities. Also, the financial support received from the Mitacs Accelerate Program (Grant No. IT17218) is acknowledged.

Data availability No data was used for the research described in the article.

Declarations

Competing interests The authors declare no competing interests.

References

1. Nadella R, Eskin DG, Du Q, Katgerman L (2008) Macrosegregation in direct-chill casting of aluminium alloys. Prog Mater Sci 53(3):421–480
2. Janeček M, Margarita S, Hájek M (2004) Structural transformations in continuously cast Al-Mg alloys. J Alloys Compd 378(1-2):316–321
3. Yin S, Howells A, Lloyd DJ, Gallerneault M, Fallah V (2022) Thin strip vs direct chill casting: the effects of casting cooling rate on the As-cast microstructure of AA6005 Al-Si-Mg alloy. Metall Mater Trans A 53(6):1928–1933
4. Birol Y (2008) Recrystallization of a supersaturated Al-Mn alloy. Scr Mater 59(6):611–614
5. Wen W, Liu WC, Morris JG (2004) The effect of precipitation of Mg2Al3 and of MnAl6 on texture evolution during isothermal annealing and subsequently on formability of CC AA5182 Al alloy. Mater Sci Eng A 380:191–207
6. Glenn AM, Russo SP, Paterson PJK (2003) The effect of grain refining on macrosegregation and dendrite arm spacing of direct chill cast AA5182. Metall Mater Trans A 34:1513–1523
7. Roth R, Clark J, Kelkar A (2001) Automobile bodies: can aluminum be an economical alternative to steel? JOM 53(8):28–32
8. Grasserbauer J, Weißensteiner I, Falkinger G, Kremmer TM, Uggowitzer PJ, Pogatscher S (2021) Influence of Fe and Mn on the microstructure formation in 5xxx alloys-part I: evolution of primary and secondary phases. Materials 14:3204
9. Li YJ, Arnberg L (2004) Solidification structures and phase selection of iron-bearing eutectic particles in a DC-cast AA5182 alloy. Acta Mater 52(9):2673–2681
10. Zha M, Li Y, Mathiesen RH, Bjørge R, Roven HJ (2013) Annealing response of binary Al-7Mg alloy deformed by equal channel angular pressing. Mater Sci Eng A 586:374–381
11. Okamoto H, Schlesinger ME, Mueller EM (2016) Al (aluminum) binary alloy phase diagrams, Alloy phase diagrams. ASM International, pp 113–139
12. Qiu Y, Yang X, Xu J, Li J, Xiang S, Chen Z, Sanders RE Jr (2022) Enhanced mechanical property and corrosion resistance of alloy 5182 FSW joints by Sc and Zr alloying. Mater Charact 194:112412
13. Zhang R, Knight SP, Holtz RL, Goswami R, Davies CHJ, Birbilis N (2016) A survey of sensitization in 5xxx series aluminum alloys. Corrosion 72:144–159
14. Foley DL, Leff AC, Lang AC, Taheri ML (2020) Evolution of β-phase precipitates in an aluminum-magnesium alloy at the nanoscale. Acta Mater 185:279–286
15. Parente M, Safdarian R, Santos AD, Loureiro A, Vilaca P, Natal Jorge RM (2016) A study on the formability of aluminum tailor welded blanks produced by friction stir welding. Int J Adv Manuf Technol 83:2129–2141
16. Bozzi S, Helbert-Etter AL, Baudin T, Klosek V, Kerbiguet JG, Criqui B (2010) Influence of FSSW parameters on fracture mechanisms of 5182 aluminium welds. J Mater Process Technol 210:1429–1435
17. Soundararajan V, Yarrapareddy E, Kovacevic R (2007) Investigation of the friction stir lap welding of aluminum alloys AA5182 and AA6022. J Mater Eng Perform 16:477–484
18. Leitao C, Emílio B, Chaparro BM, Rodrigues DM (2009) Formability of similar and dissimilar friction stir welded AA 5182-H111 and AA 6016-T4 tailored blanks. Mater Des 30(8):3235–3242
19. Jin H, Saimoto S, Ball M, Threadgill PL (2001) Characterisation of microstructure and texture in friction stir welded joints of 5754 and 5182 aluminium alloy sheets. Mater Sci Technol 17(12):1605–1614
20. Miles MP, Nelson TW, Decker BJ (2004) Formability and strength of friction-stir-welded aluminum sheets. Metall Mater Trans A 35:3461–3468
21. Baudin T, Bozzi S, Brisset F, Azzeddine H (2023) Local microstructure and texture development during friction stir spot of 5182 aluminum alloy. Crystals 13(3):540
22. McMahon ME, Haines RL, Steiner PJ, Schulte JM, Fakler SE, Burns JT (2020) Beta phase distribution in Al-Mg alloys of varying composition and temper. Corros Sci 169:108618
23. D'Antuono DS, Gaies J, Golumbfskie W, Taheri ML (2014) Grain boundary misorientation dependence of β phase precipitation in an Al–Mg alloy. Scr Mater 76:81–84
24. Heidarzadeh A, Mironov S, Kaibyshev R, Çam G, Simar A, Gerlich A, Khodabakhshi F, Mostafaei A, Field DP, Robson JD, Deschamps A, Withers PJ (2021) Friction stir welding/processing of metals and alloys: a comprehensive review on microstructural evolution. Prog Mater Sci 117:100752
25. Sahu M, Paul A, Ganguly S (2022) Influence of frictional heat spread pattern on the formation of intermetallic layers at the dissimilar FSW joint interface between AA 5083 and HSLA steel. J Manuf Process 83:555–570
26. Hou W, Ding Y, Huang G, Huda N, Shah LHA, Piao Z, Shen Y, Shen Z, Gerlich A (2022) The role of pin eccentricity in friction stir welding of Al-Mg-Si alloy sheets: microstructural evolution and mechanical properties. Int J Adv Manuf Technol 121:7661–7675
27. Pouraliakbar H, Beygi R, Fallah V, Hosseini Monazzah A, Jandaghi MR, Khalaj G, da Silva LFM, Pavese M (2022) Processing of Al-Cu-Mg alloy by FSSP: parametric analysis and the effect of cooling environment on microstructure evolution. Mater Lett 308:131157
28. Mazaheri H, Aval HJ, Jamaati R (2021) Pre-strain assisted low heat-input friction stir processing to achieve ultrafine-grained copper. Mater Sci Eng A 826:141958
29. Ahmed MMZ, Ataya S, El-Sayed Seleman MM, Mahdy AMA, Alsaleh NA, Ahmed E (2021) Heat input and mechanical properties investigation of friction stir welded AA5083/AA5754 and AA5083/AA7020. Metals 11:68
30. Prasad Y, Rao K, Sasidhar S (eds) (2015) Hot working guide: a compendium of processing maps. ASM International
31. Bayazid SM, Heddad MM, Cayiroglu I (2018) A review on friction stir welding, parameters, microstructure, mechanical properties, post weld heat treatment and defects. Mater Sci Eng 2(4):116–126
32. Siddiquee AN, Khan ZA, Shihab SK (2015) Investigations on tunneling and kissing bond defects in FSW joints for dissimilar aluminum alloys. J Alloys Compd 648:360–367

33. Guan W, Li D, Cui L, Wang D, Wu S, Kang S, Wang J, Mao L, Zheng X (2021) Detection of tunnel defects in friction stir welded aluminum alloy joints based on the in-situ force signal. J Manuf Process 71:1–11
34. Grasserbauer J, Weißensteiner I, Falkinger G, Uggowitzer PJ, Pogatscher S (2021) Influence of Fe and Mn on the microstructure formation in 5xxx alloys-part II: evolution of grain size and texture. Materials 14:3312
35. Liu Y, Luo L, Han C, Ou L, Wang J, Liu C (2016) Effect of Fe, Si and cooling rate on the formation of Fe- and Mn-rich intermetallics in Al-5Mg-0.8Mn alloy. J Mater Sci Technol 32(4):305–312
36. Li YJ, Arnberg L (2004) A eutectoid phase transformation for the primary intermetallic particle from Alm(Fe,Mn) to Al3(Fe,Mn) in AA5182 alloy. Acta Mater 52(10):2945–2952
37. Straumal B, Korneva A, Kuzmin A, Klinger L, Lopez GA, Vershinin N, Straumal A, Gornakova A (2022) High entropy alloys for energy conversion and storage: a review of grain boundary wetting phenomena. Energies 15(19):7130
38. Straumal B, Kogtenkova O, Bulatov M, Nekrasov A, Baranchikov A, Baretzky B, Straumal A (2021) Wetting of grain boundary triple junctions by intermetallic delta-phase in the Cu-In alloys. J Mater Sci 56:7840–7848
39. Chang C, Lee C, Huang J (2004) Relationship between grain size and Zener-Holloman parameter during friction stir processing in AZ31 Mg alloys. Scr Mater 51(6):509–514
40. Zhu Y, Cullen DA, Kar S, Free ML, Allard LF (2012) Evaluation of Al3Mg2 precipitates and Mn-rich phase in aluminum-magnesium alloy based on scanning transmission electron microscopy imaging. Metall Mater Trans A 43(13):4933–4939
41. Nakamura T, Obikawa T, Nishizaki I, Enomoto M, Fang Z (2018) Friction stir welding of non-heat-treatable high-strength alloy 5083-O. Metals 8(4):208
42. Oguocha INA, Adigun OJ, Yannacopoulos S (2008) Effect of sensitization heat treatment on properties of Al-Mg alloy AA5083-H116. J Mater Sci 43:4208–4214
43. Qiu Y, Yang X, Li J, Xiang S, Shi J, Xu J, Sanders RE (2022) The influence of Sc and Zr additions on microstructure and corrosion behavior of AA5182 alloy sheet. Corros Sci 199:11081
44. Yilmaz A (2011) The Portevin-Le Chatelier effect: a review of experimental findings. Sci Technol Adv Mater 12(6):063001
45. Cho CH, Son HW, Lee JC, Son KT, Lee JW, Hyun SK (2020) Effects of high Mg content and processing parameters on Portevin-Le Chatelier and negative strain rate sensitivity effects in Al-Mg alloys. Mater Sci Eng A 779:139151
46. Rowlands BS, Rae C, Galindo-Nava E (2022) The Portevin-Le Chatelier effect in nickel-base superalloys: origins, consequences and comparison to strain ageing in other alloy systems. Prog Mater Sci 132:101038
47. Zhang Y, Liu JP, Chen SY, Xie X, Liaw PK, Dahmen KA, Qiao JW, Wang YL (2017) Serration and noise behaviors in materials. Prog Mater Sci 90:358–460
48. Hirosuke I, Komatsubara T (2000) Yield point elongation in Al-Mg alloys. Mater Sci Forum 331-337:1303–1308